Renewable Energy 131 (2019) 1255–1273

Contents lists available at ScienceDirect

Renewable Energy

journal homepage: www.elsevier.com/locate/renene

Numerical study of effect of winglet planform and airfoil on a horizontal axis wind turbine performance

A. Farhan, A. Hassanpour*, A. Burns, Y. Ghaffari Motlagh

School of Chemical and Process Engineering, University of Leeds, LS2 9JT, UK

ARTICLE INFO

Article history:
Received 29 January 2018
Received in revised form
15 July 2018
Accepted 5 August 2018
Available online 10 August 2018

Keywords:
Aerodynamics
CFD
Wind turbine
Winglet
Wingtip vortices

ABSTRACT

Winglets can reduce effect of wingtip vortices on the wind turbine performance can be reduced by diffusing the vortices from the blade tips. Unlike non-rotating wings, winglets have not been widely investigated for moving blades of wind turbines, while there is a potential they could enable the wind turbine rotor to capture more kinetic energy from wind. There have been a number of studies on the effect of winglet parameters and configurations on the wind turbine performance, however a combined effect of winglet planform and airfoil has not been investigated in details. The present work reports on the study of the effect of winglet planform and winglet airfoil on the wind turbine performance using Computational Fluid Dynamics (CFD). The National Renewable Energy Laboratory (NREL) phase VI rotor with 10 m diameter was used as the baseline and the CFD results were validated with the available experimental data on the output power and pressure coefficients. Different designs of winglet with different heights, cant angles, planforms and airfoils have been numerically tested and optimised. The best improvement in the performance is achieved when a 15 cm rectangular winglet with the S809 airfoil and 45° cant angle is used.

1. Introduction

Global warming and the upsurge in greenhouse emissions have been the main drive and motivation for developing alternative sources of energy over fossil fuels. In particular, significant attention is being paid to renewable and pollution-free energies, such as solar energy and wind. Wind is one of the most important sources of renewable energy and it could be potentially supporting global electricity by more than 20% by 2030 [1].

Numerous researchers have studied the aerodynamic behaviour of the flow field around wind turbines to gain a better understanding of how the rotor extracts the kinetic energy of the wind. Wind tunnel experiments are notmally implemented to analyse the aerodynamic behaviour of a wind turbine at different operating conditions. However, the flow field around wind turbine is very complicated due to turbulence generation, vortices and stall flow at different operating conditions, therefore more advanced and sophisticated measurement techniques for wind tunnel tests are required. Alternatively, aerodynamic models have been used to analyse the flow field around wind turbine to address the aforementioned shortcoming in the experiments.

According to the literature, Blade Element Momentum (BEM), Vortex Method (VM) and Computational Fluid Dynamic (CFD) are common approaches that are used to calculate the aerodynamic forces [2]. BEM is a basic approach to design a rotor based on the combination of momentum and blade element theories by dividing the wind turbine blades into independent elements. A set of equations are produced which are solved iteratively by balancing axial and angular momentum for each element. A deficiency of this method is that for heavy loaded conditions, when the axial induction factor is greater than 0.5, the classical BEM theory fails to accurately predict the wind velocity in the far wake flow due to the existing turbulence and recirculation flow [3]. In this situation, the BEM predicts the wake flow velocity as a negative value, which is unreasonable [4]. Hence, the classical BEM theory should involve a number of empirical models, with a view to improve the relationship between the thrust coefficient and axial induction factor [5].

It is proven that due to the dynamic stall effects, the aerodynamic coefficients are significantly influenced by the rotational effects [6]. Zhang [7] reported that the BEM fails to match the measured shaft torque when the wind speed is higher than 7 m/s due to the dominant rotational effects. In the stall conditions, the

* Corresponding author.
E-mail address: a.hassanpour@leeds.ac.uk (A. Hassanpour).

https://doi.org/10.1016/j.renene.2018.08.017
0960-1481/

rotor is more efficient in producing power, predicted by models based on two-dimensional airfoil characteristics [8,9].

Further, addressing tip losses are considered as big challenges and can cause uncertainty in the prediction of BEM. Therefore, a number of correction factors are used to improve the classical BEM analysis, such the Prandtl's tip loss correction [10]. In addition, other tip loss corrections have been derived in different work which are summarised by Shen, Mikkelsen [11]. In general, the major drawback of the model is its dependency on the empirical correction, which are not always available to the requirements of all operating conditions such as misalignment, dynamic stall, tower influence and finite number of blades [12].

Unlike BEM methods, VM implements a more sophisticated approach to model the flow field around the wind turbine by assuming that the flow field is inviscid. According to VM, the wind turbine blade and wake are modelled by vortex particles or vortex filaments where the rotor is modelled by the lifting line, lifting surface or the panel method. The lifting line method is based on Prandtl's lifting line theory where the blade is divided into a number of sections. Each section is modelled by a straight vortex filament of constant strength. Using the available aerodynamic data for lift (Cl) and drag (Cd) coefficients verses the angle of attack, wind turbine output power and torque can be calculated. Interestingly, the VM intrinsically predicts the effects of tip vortices and does not need to be corrected by implementing tip loss factors [13]. However, these methods do not have the potential to predict the flow separation and rely on existing data on Cl and Cd [14].

On the other hand, due to a rapid improvement in computational power, CFD has become an attractive method in diverse engineering fields as it can solve the Navier-Stokes (N–S) equations which are based on the conservation of mass, momentum and energy. The major advantage of this method is that, CFD has the potential to effectively describe the behaviour of flow as laminar, transitional or turbulent. Moreover, it can deal with different turbulence models in different conditions. In addition, CFD can present the output results of streamlines, pressure and velocity contours as actual flow around a wind turbine without the need of using previously reported Cl and Cd values [15]. Recently, CFD has been used as the main tool to predict the Horizontal Axis Wind Turbine (HAWT) performance because of its potential to model the 3D effects, for instance turbulence phenomenon, stall flow, yawed factor and providing detailed flow inside boundary layers.

In the last few years, many researchers investigated the improvement of wind turbine output by studying the aerodynamic characteristics of wind turbine blades. Vortices are considered a source to generate the induced drag and reduce the lift force. The main function of winglets attached to the blade is to reduce the effect of the wingtip vortices which are generated due to the 3D spanwise flow that occurs because of the pressure non-equalization between the upper and lower blade surfaces. Furthremore, any extension of a blade that significantly influences the fluid flow could potentially extract more available energy. Accordingly, the winglet planform and airfoil play significant roles in extracting additional available energy from the fluid flow in addition to reduction of the impact of the wingtip vortices by shifting them away from the blade tip to the winglet tip. Unlike non-rotating wings, winglet parameters have not been fully investigated for rotating wings, i.e. wind turbines. Maughmer [16] stated that, the most important winglet parameters that should be studied are planform shape, winglet height, sweep, twist, toe and cant angles where each parameter plays a different role in improving a winglet performance. A planform shape is employed to control the spanwise flow to minimise the effect of induced drag. Additionally, winglet height and planform increase a profile drag which significantly affects the winglet performance [17]. Meanwhile, the winglet sweep and twist angles are responsible for the load distribution on the winglet planform to avoid the stalled flow on a winglet. Further, the toe angle controls the aerodynamic effect of the winglet on the load distribution along a wing [18]. Whereas, the cant angle controls the upwards or downwards flow direction on a wing.

In the literature, there are a number of studies that used the CFD methods to solve the governing equations that control flow around the wind turbine and to investigate the effect of winglet parameters. Elfarra, Sezer Uzol [19] studied the aerodynamic impact of four rectangular winglets by optimising cant and twist angles. The study shows that, the wind turbine performance increased by 9% when using a winglet that was extended by 1.5% of the blade length and tilted towards the suction side with 45° and 2° cant and twist angles, respectively. Gupta and Amano [20] investigated the influence of the winglet height and cant angle on the wind turbine output power. A 20% increase in the output power was established by a winglet with the cant angle of 45° and extending height by 4% of the blade length. Congedo and De Giorgi [21] studied the optimisation of the winglet height and the curvature radius. Their results show that, increasing the curvature radius of the winglet by 50% leads to a slight increase in the mechanical power by 1.6%, and by 1.7% when increasing the winglet height by 25%. Johansen and Sørensen [22] reported the winglet influences on mechanical power and thrust force. Different rectangular winglet parameters such as winglet height, curvature radius, sweep and twist angles were considered and optimised. The results showed that an increase of the twist angle from 0° to 8° leads to 1.6% increase in the mechanical power and 1.9% in the thrust force. However, the greatest increase was achieved by the configuration which was bent toward the suction side and twisted by -2°. The increase in mechanical power was 1.71%, at a wind speed 10 m/s. Ali [23] examined the effect of the rectangular winglet position (upwind and downwind) on small wind turbine performance experimentally. The experimental results showed that the maximum power coefficient was 0.48 as a result of adding the upwind winglet, whereas the baseline produced 0.45. In contrast, the downwind winglet caused a drop in the maximum power coefficient from 0.45 (baseline) to 0.41. Other researchers investigated effect of winglet shape on the wind turbine performance. Ariffudin and Zawawi [24] reported the comparison between two tip extensions (sword and swept) and rectangular winglet shapes that have 20 mm length and tilted by 83° cant angle toward the upwind and downwind directions. The results showed that both the tip extensions perform better than winglet configurations. Gertz [18] investigated the effect of winglet planform where rectangular and elliptical winglets were created using the PSU 94–097 airfoil. Both winglets were pointed by a 90° cant angle and the winglet height was 8% of the baseline blade toward the suction side. The winglet parameters were taken from previous literature and Maughmer's recommendations. The study showed both winglets increased the power output by 5%, at wind speeds between 6.5 m/s to 9.5 m/s when compared to the baseline case. However, the wind turbine output decreased beyond this wind speed range. This is probably due to the reason that the length of winglet has significant effect on the profile drag at high wind speeds and this was not investigated by the author.

Despite extensive previous studies on the winglet parameters according to Maughmer's recommendations [16], the combined influence of winglet planform and winglet airfoil on the performance has not been investigated in detail.

This paper investigates the effect of winglet planform and winglet airfoil on the NREL phase VI performance as they play significant roles in diffusing wingtip vortices. For this purpose, two winglet planforms, the rectangular and elliptical, are examined. Moreover, the effect of airfoil on the winglet performance is studied by employing the S809 and PSU 94–097 airfoils for the profile of winglets.

The CFD tool was chosen to model the flow field around the NREL phase VI rotor and the validation was done by comparing the calculated output power and pressure coefficients with the measured data.

2. NREL phase VI configuration

The NREL phase VI rotor geometry was chosen as a baseline case to validate the CFD results. This rotor was tested experimentally in a wind tunnel (24.4 × 36.6 m) at NASA's Ames Research Centre. The NREL phase VI rotor is an upwind horizontal axis wind turbine and consists of two tapered and twisted blades that are constructed using S809 airfoil as shown in Fig. 1. The specifications of the blade and the rotor parameters are shown in Table 1 [25].

3. Governing equations

The main concept of CFD is to solve the fundamental equations of the fluid dynamics which are known as the Navier-Stokes equations. The Navier-Stokes equations are based on the conservation laws; known as the conservation of mass, momentum and energy as defined in the following [26].

$$\frac{\partial \rho}{\partial t}+\frac{\partial}{\partial x}(\rho u)+\frac{\partial}{\partial y}(\rho v)+\frac{\partial}{\partial z}(\rho w)=0 \tag{1}$$

$$\rho\frac{Du}{Dt}=\frac{\partial(-p+\tau_{xx})}{\partial x}+\frac{\partial \tau_{yx}}{\partial y}+\frac{\partial \tau_{zx}}{\partial z}+S_{Mx} \tag{2}$$

$$\rho\frac{Dv}{Dt}=\frac{\partial \tau_{xy}}{\partial x}+\frac{\partial(-p+\tau_{yy})}{\partial y}+\frac{\partial \tau_{zy}}{\partial z}+S_{My} \tag{3}$$

$$\rho\frac{Dw}{Dt}=\frac{\partial \tau_{xz}}{\partial x}+\frac{\partial \tau_{yz}}{\partial y}+\frac{\partial(-p+\tau_{zz})}{\partial z}+S_{Mz} \tag{4}$$

where

u, v and w = components of the velocity in the x, y and z direction respectively.
p = pressure.
τ_{ij} = the normal and shear stresses that affect the 3D fluid particles.

Fig. 1. The NREL Phase VI rotor geometry [25].

Table 1
Specifications of the NREL phase VI rotor.

Number of blades	2
Rotor diameter	10.058
RPM	72
Rotor location	Upwind
Power regulation	Stall regulated
Pitch angle	3°
Output power	20 kW
Profile of blade	S809
Twist angle	Non-liner twist along the span
Blade thickness	21% throughout the span
Cone angle	0°
Blade chord length	0.728m-0.358 m (linearly tapered)

S_{Mx}, S_{My} and S_{Mz} = body forces per unit of mass in the x, y and z direction.

Based on the Reynolds decomposition, additional turbulent stresses occur in the Reynolds Averaged Navier Stokes (RANS) which are written as follows.

$$\frac{\partial \rho}{\partial t}+\frac{\partial}{\partial_{x_i}}(\rho u_i)=0 \tag{5}$$

$$\frac{\partial}{\partial t}(\rho u_i)+\frac{\partial}{\partial x_j}(\rho u_i u_j)=-\frac{\partial p}{\partial x_i}+\frac{\partial}{\partial x_j}\left[\mu\left(\frac{\partial u_i}{\partial x_j}+\frac{\partial u_j}{\partial x_i}-\frac{2}{3}\delta_{ij}\frac{\partial u_i}{\partial x_j}\right)\right]+\frac{\partial}{\partial x_j}\left(-\rho\overline{u_i' u_j'}\right) \tag{6}$$

In this study, the Spalart-Allmaras and $k-w$ *SST* models were used to close the RANS equations.

4. Methodology

In this work, the Moving Reference Frame (MRF) approach was chosen to model the flow field around a wind turbine. The MRF is a steady-state approximation model that permits an unsteady stationary frame to be steady with respect to the moving frame where different rotational and/or translational speeds can be specified for different zones [27]. A comparative study was performed on different domain sizes by varying the downstream distance as 2.5D, 4D, 6D while keeping the upstream distance as D (Fig. 2a). From Fig. 2a, the 2.5D domain was chosen an optimum domain size where the predicted torque agrees reasonably with the wind tunnel data at wind speeds of 5 m/s and 7 m/s. In fact the wind tunnel size in experiment is 2.5D which is probably the main reason for this agreement. In addition, the same validated numerical results were obtained in a number of studies which utilised the current domain size [28,29]. Further, similar match to experimental data was achieved in a number of investigations that implemented a downstream distance of more than 4D [30,31].

The domain is divided into a rectangular domain that is located and rotating cylindrical domain that is close to the blades, while the interface boundary condition was used to merge the separated frames as shown in Fig. 2b. Uniform wind speeds were applied from 5 m/s to 25 m/s at the inlet of the computational domain and the gage pressure was assigned to zero at the outlet of domain. The no-slip shear condition and rotating wall were imposed to define the rotor blades while the wall of the rectangular domain was defined stationary with no-slip condition.

An unstructured mesh was used to discretize both zones using a mesh generator (Ansys 17.0) as shown in Figs. 3 and 4. In addition,

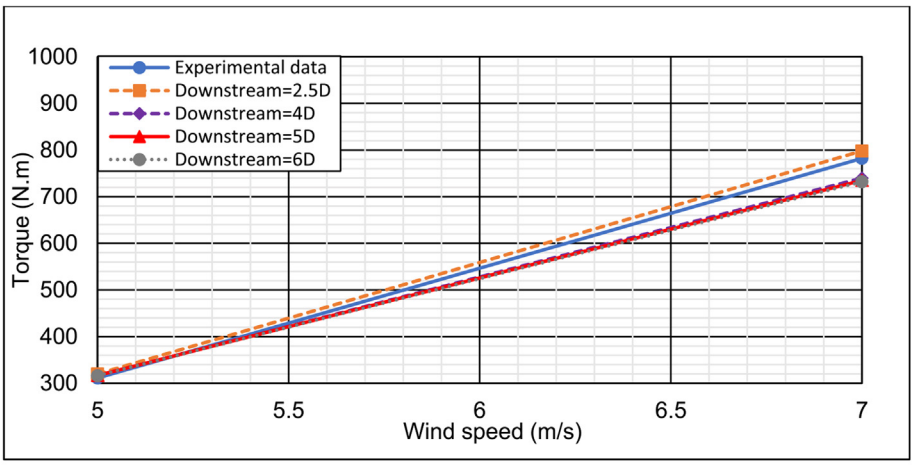

(a)

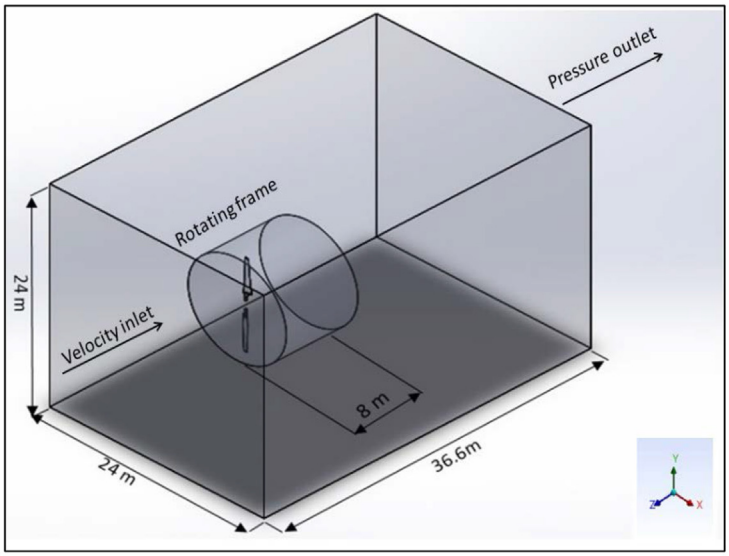

(b)

Fig. 2. (a) Assessment of computational domain sizes. (b) Schematic diagram of the chosen computational domain.

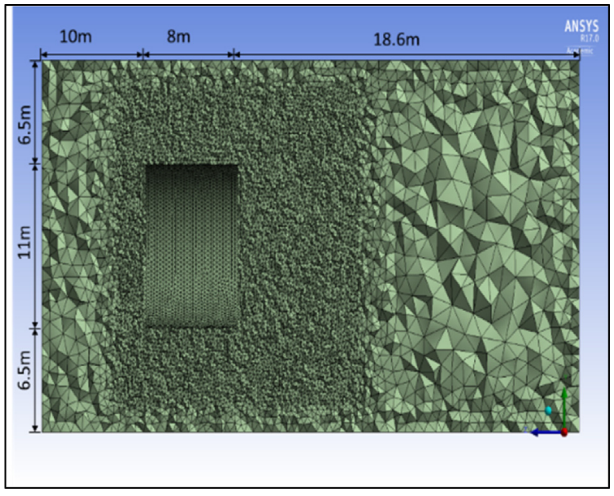

Fig. 3. View of the unstructured grid in stationary domain.

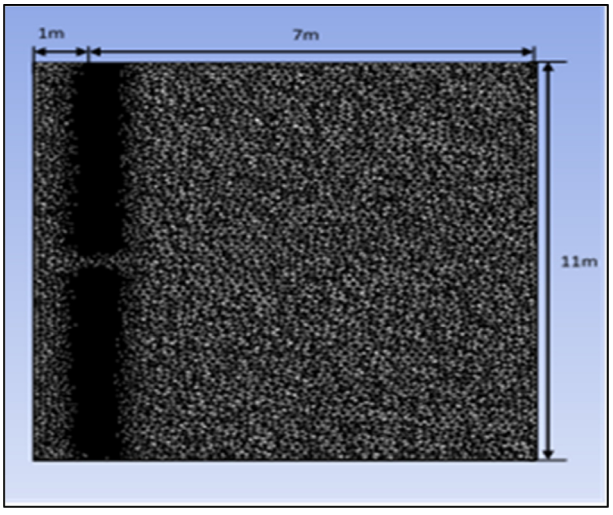

Fig. 4. View of the unstructured grid in rotating domain.

to integrate the partial differential equations from the viscous sublayer without using wall function, the meshes were generated with y + less than 2 near the wall, with 10 prism layers close to the blade surface. The steady state CFD simulation, RANS equations and two different turbulence models including Spalart-Allmaras and Shear Stress Transport (SST) K-ω were implemented using Ansys Fluent 17.0. The second order upwind schemes were utilised to discretize the convection terms and the SIMPLE algorithm was used for the pressure-velocity coupling. The solution convergence was established by monitoring the residual history, moment and lift coefficients over 2000 iterations. However, an adequate convergence was noticed after 1200 iterations when the convergence criteria were 10^{-6} for all variables.

5. Numerical results

The numerical calculations have been performed using the commercial general-purpose software Ansys-Fluent 17.0. The CFD results were divided into two parts. A validation part was done to assess the capability of the computational model to predict the experimental data of the NREL phase VI rotor published by the NREL. The second part is the numerical results that were obtained by attaching different winglet planforms. The validation was carried out by comparing the wind turbine aerodynamic power, normal force coefficients and distribution of pressure coefficients with the measured data for different wind speeds at different spanwise sections along the wind turbine blade. Fig. 5 shows the comparison of computed power obtained using two different turbulence models with the measured power of the NREL phase VI rotor. The output power was calculated by monitoring the torque around a rotating axis and multiplying it with the angular velocity using Eq. (7). Grid independence analysis was carried out on the numerical torque values at the wind speeds of 5 m/s and 7 m/s by the refinement of mesh around the blade surface as shown in Fig. 6.

$$\boldsymbol{P} = \boldsymbol{T}^{*}\boldsymbol{\omega} \tag{7}$$

where

P: computed output power (W).
T: torque (N.m).
ω: angular velocity (rad/s).

From Fig. 5, it can be observed that, there is a good agreement between the computed power and the measured data at low and moderate wind speeds between 5 and 8 m/s. However, the Spalart-Allmaras model overpredicted the output power at high wind speeds due to a stall regime that occurs at the wind speeds of 11 m/s to 25 m/s. Unlike Spalart-Allmaras model, the K-ω (SST) model shows better performance to capture the flow parameters at the pre-stall and stall regimes. This result is expected as different techniques are followed by each model to predict the turbulence effects. However, the SST model shows about 11 % discrepancy comparing to the experimental data for the wind speeds 9–11 m/s. The reason for this discrepancy might be due to the effect of the transition flow which occurs at wind speeds of 9 m/s to 11 m/s [32].

Spalart-Allmaras model is an economical model which solves a single transport equation to compute the kinematic eddy viscosity. The turbulence length scale is modelled using an algebraic equation. Additionally, it has been shown by other researchers that a good prediction of the flow parameters in the boundary layers with moderate pressure gradients can be obtained which are the most important aspects to predict the location of the stalled flow in the aerodynamic applications including wind turbine. The main weakness of the Spalart-Allmaras model is that, it predicts high backflow velocities in the recirculation region due to its insensitivity to the effect of adverse pressure gradients [33].

On the other hand, the SST model is a two-equation hybrid method, that combines two different turbulence models of k-ω and k-ε by using a blending function that implements the k-ω model

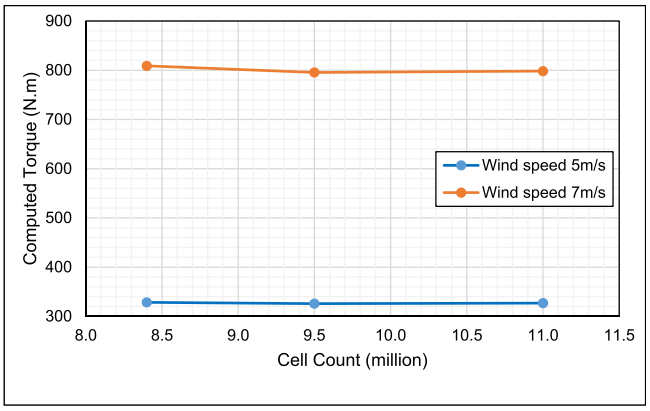

Fig. 6. Effect of grid refinement on the computed torque.

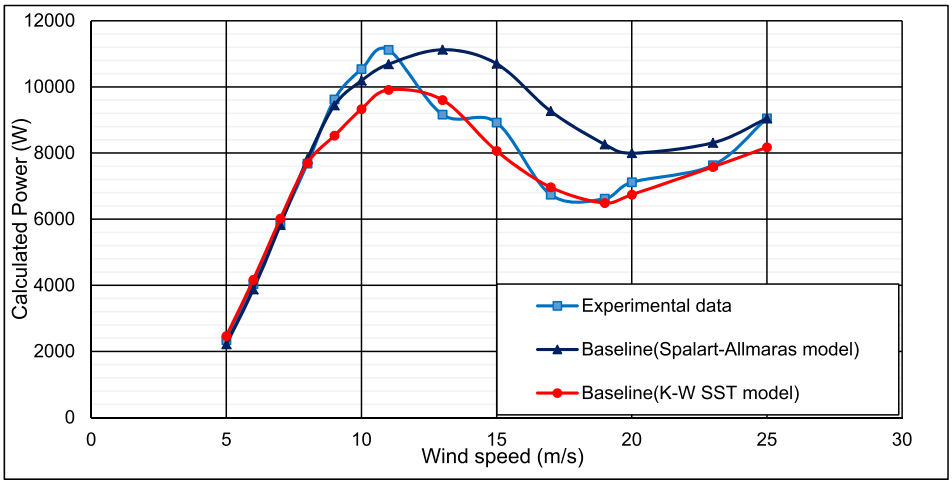

Fig. 5. Comparison of measured and calculated power using couple turbulence models.

near the wall and gradually converting to the k-ε model in the regions sufficiently far away from the wall.

Hence, it is able to capture the separated flow that occurs at the wind speeds above 10 m/s more accurately. Therefore, in this work the SST model was used to simulate the baseline rotor with all winglet designs.

Figs. 7–9 show the comparisons of measured and calculated pressure coefficients and normal force coefficients for wind speeds of 7, 10 and 25 m/s at 30%, 47%, 63%, 80% and 95% spanwise sections of the blade, respectively. The pressure coefficients and normal force coefficients were calculated as follows.

$$C_p = \frac{P - P_\infty}{\frac{1}{2}\rho\left(U_\infty^2 + (\omega r)^2\right)} \tag{8}$$

where,

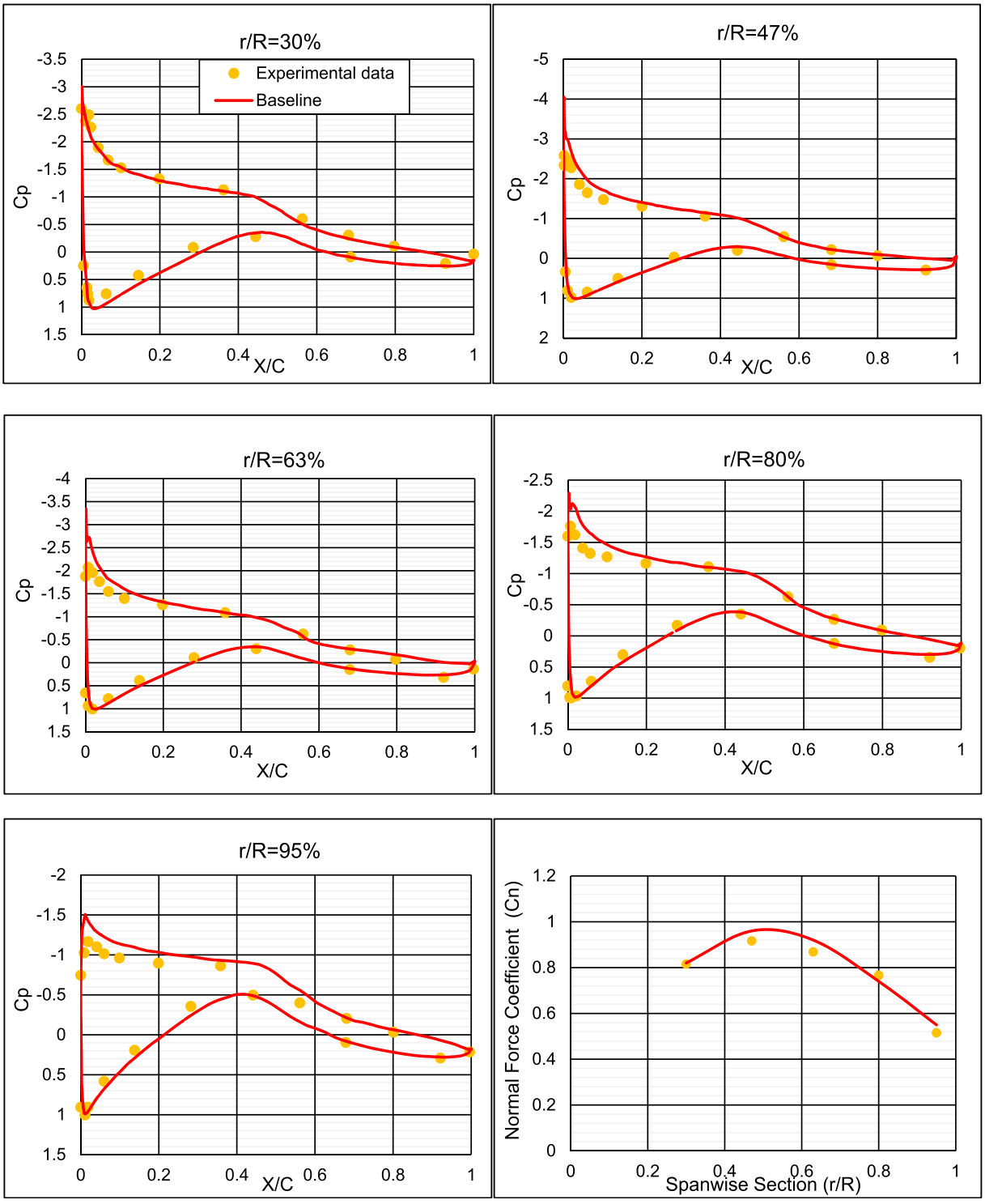

Fig. 7. Comparison of CFD and measured coefficients (pressure and normal force) at 7 m/s.

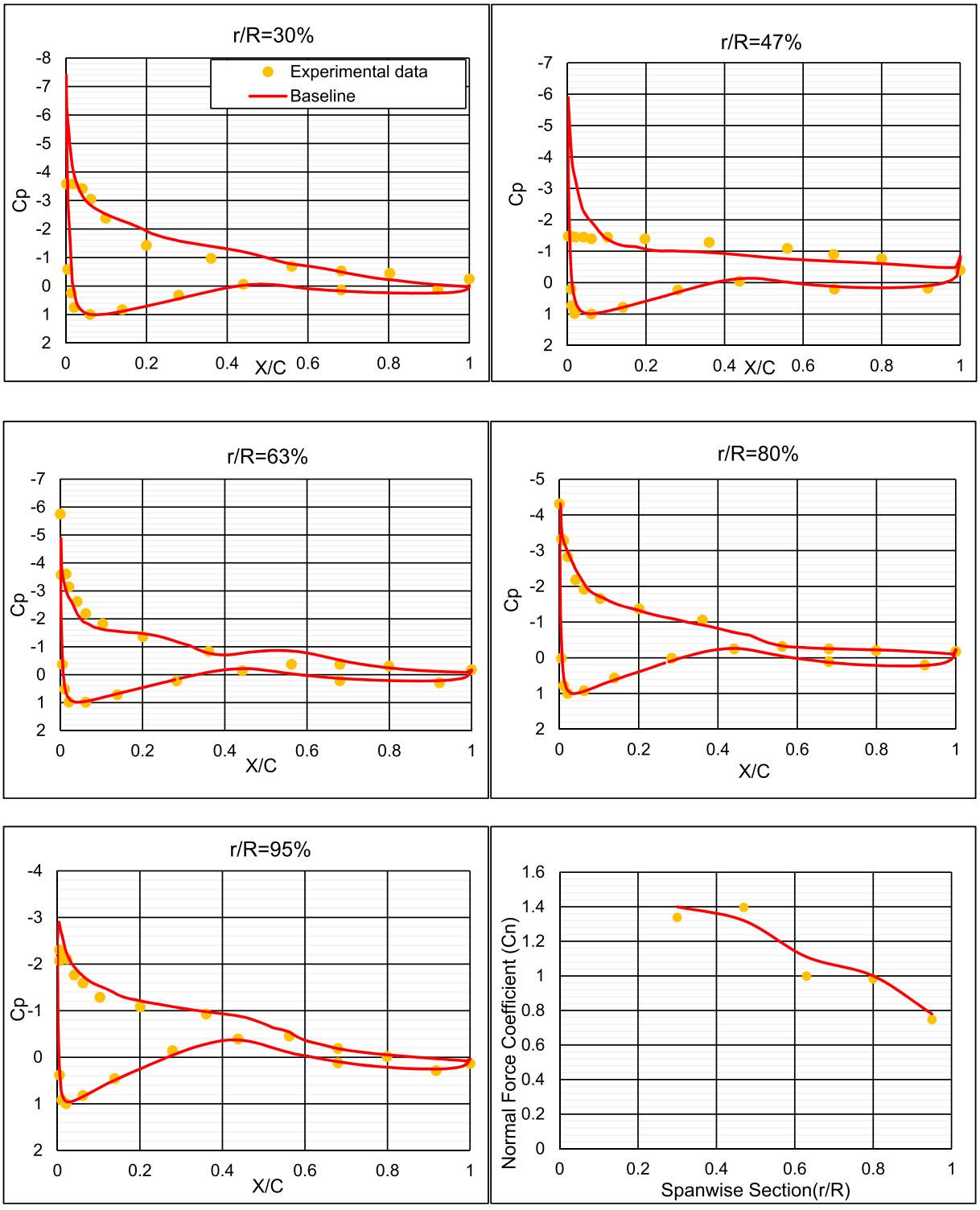

Fig. 8. Comparison of CFD and measured coefficients (pressure and normal force) at 10 m/s.

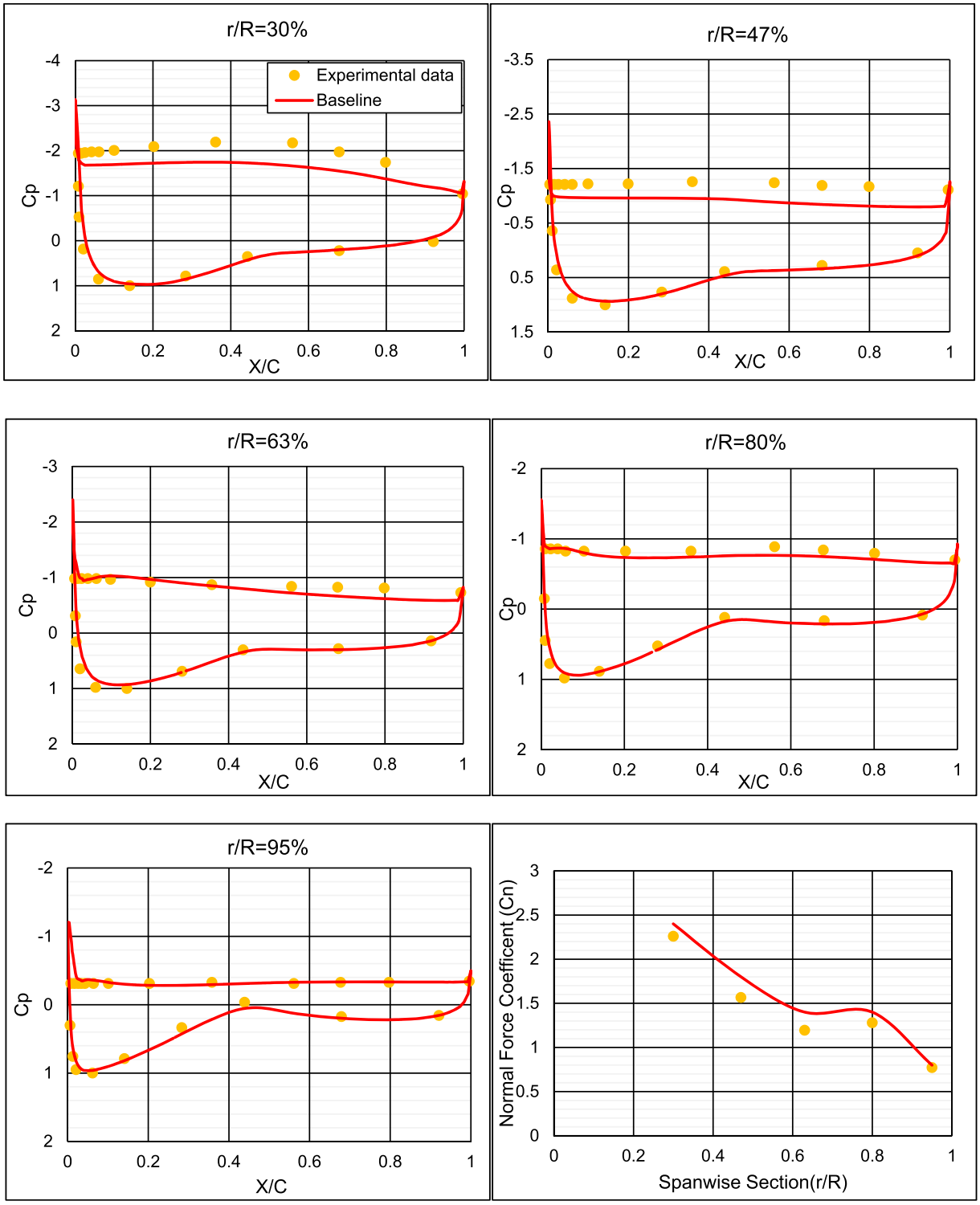

Fig. 9. Comparison of CFD and measured coefficients (pressure and normal force) at 25 m/s.

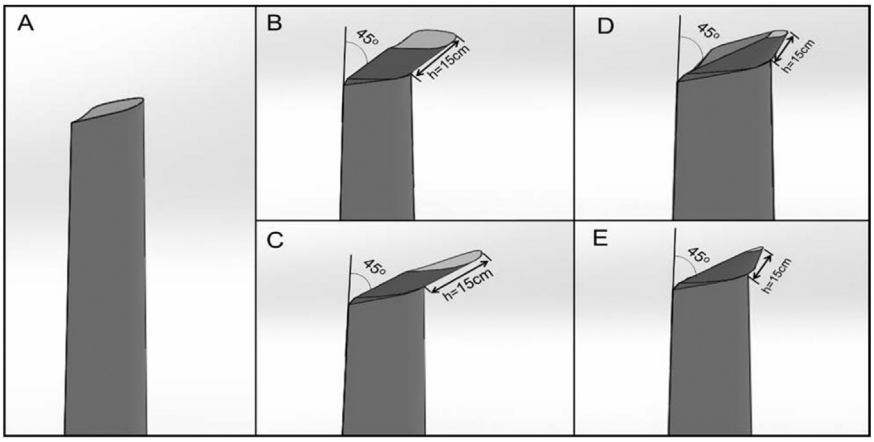

Fig. 10. A-Baseline blade B-Rectangular (S809) C- Rectangular (PSU 94–097) D-Elliptical (S809) E- Elliptical (PSU 94–097).

P: computed local static pressure. U_∞: wind speed [m/s]. P_∞: Free-stream static pressure. ω : Angular velocity [rad/s]. ρ: Free stream density [Kg/m^3]. r: radial distance from the hub centre to the blade section [m].

And

$$C_n = \sum_i \left(\frac{C_{pi} + C_{pi+1}}{2} \right) (x_{i+1} - x_i) \quad (9)$$

where,

C_{pi}: The normalized calculated pressure coefficient.
x_i : The normalized distance along the chord line.

At low and moderate wind speeds of 7 and 10 m/s, it could be noticed that good agreements were obtained with the measured results at all spanwise sections for pressure and normal force coefficients where there is no stall at these wind speeds. However, it is clear from Fig. 9 that there is a discrepancy between the measured and computed pressure coefficient distributions and normal force coefficients at 25 m/s, particularly in the suction side. The discrepancy was found in 30%, 47%, 63% and 80% spanwise sections of the blade due a strong stalled flow which occurred at this speed. Similar results were obtained by a number of researchers [34], [35] and [19].

6. Winglet configurations

In this study, the baseline blade tip shown in Fig. 10 was modified by attaching different winglet configurations. Two different winglet planforms, namely, rectangular and elliptical as shown in Fig. 10 were studied to investigate the influence of the winglet planform on the aerodynamic behviour of the blade. The rectangular winglet planform was created by extending the height of the blade tip chord; meanwhile the elliptical winglet planform was created with 75% linear reduction of the chord length from root towards the winglet tip. In addition, S809 and PSU 94–097 airfoils were chosen to create two different winglet profiles. A transition section was created to attach the baseline blade to each winglet configuration generated by the PSU 94–097 or S809 airfoil. The four winglet configuration parameters are listed in Table 2.

The S809 airfoil as shown in Fig. 11 was designed theoretically and verified experimentally for the NERL by Airfoils and Incorporated State college [36]. The S809 airfoil was tested at Reynolds numbers of 1.0×10^6 to 3.0×10^6 where fluid flow characteristics such aerodynamic coefficients, transitional flow and stall regime on the upper and lower airfoil surfaces were investigated.

In contrast, the PSU 94–097 airfoil shown in Fig. 12 was designed as a winglet airfoil at Reynolds numbers of 2.4×10^5 to 1.0×10^6 to improve the performance of sailplanes [37]. In addition, for this airfoil the requirements that satisfy its performance in a wide range of low-speed applications were considered which makes the airfoil suitable for horizontal axis wind turbines [38] and [39].

Therefore, the S809 airfoil was chosen to construct a winglet profile as it has similar aerodynamic characteristics of the baseline tip airfoil. In contrast, the function of winglet is diffusing of the wingtip vortices, which is different than the baseline blade. Meanwhile, the PSU 94–097 airfoil that was tested for low speed application was also considered in this study.

Table 2
Winglet configurations.

Configuration No.	Winglet Planform	Winglet airfoil
1	Rectangular	S809
2	Rectangular	PSU 94-097
3	Elliptical	S809
4	Elliptical	PSU 94-097

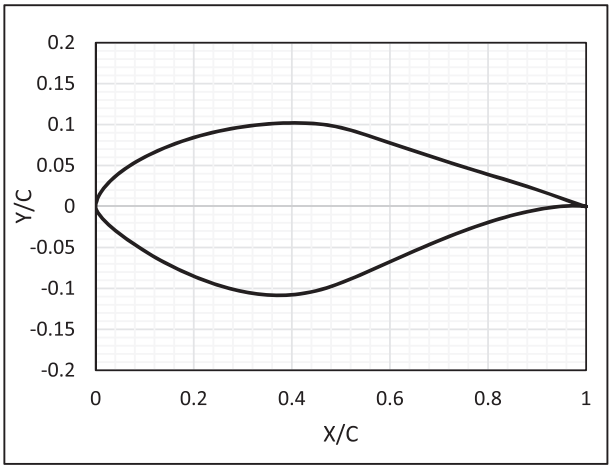

Fig. 11. Schematic of S809 airfoil.

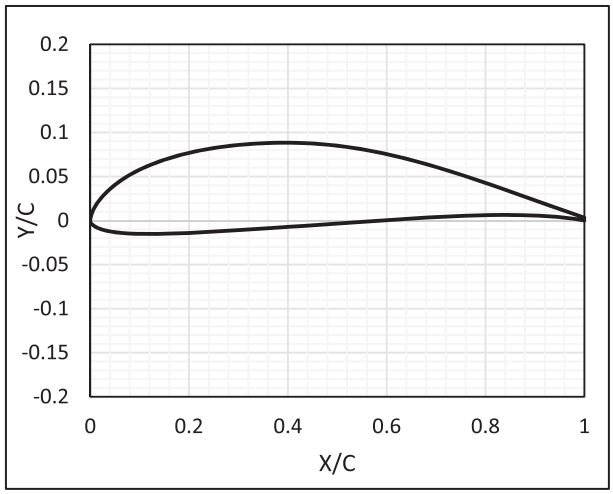

Fig. 12. Schematic of PSU 94–097 airfoil.

For winglet cases, the same mesh topology and numerical methodology that were used to assess the validation of the baseline case were followed. The overall number of cells is increased from 11 million cells to more than 13 million cells due to the addition of winglet. In addition, the effect of grid refinement on the computed torque was investigated by the refinement of cell size from 7 mm to 6 mm (increasing the overall cell number to just over 17 million cells). The refinement was applied on the configuration 1 and as a result the change in the computed torque were found to be about 0.6% and 1% at the wind speeds of 5 m/s and 7 m/s, respectively.

The winglet height and cant angle were chosen after an optimisation study based on the best performance in terms of output power at different wind speeds. The results are shown in Table 3 and it can be seen that for each configuration a 15 cm extension of the blade tip with 45° cant angle towards the suction side of the blades provides the best performance in terms of increasing the predicted output power as compared to the base line.

7. Sectional flow and surface wall shear streamlines

Figs. 13 and 14 show the influence of configurations 1 and 3 (effect of planform shape with fixed airfoil) on the cross-sectional flow and surface wall streamlines at the wind speeds of 7 m/s and 15 m/s. Considering the spanwise direction, there is no significant effect on the flow behaviour at the five spanwise sections of the baseline blade for the cases of 7 m/s and 15 m/s.

In contrast, the influence of configurations 1 and 3 can be clearly observed by presenting the skin friction streamlines at the wind speeds of 7 m/s and 15 m/s as shown in Figs. 15 and 16, respectively.

At 7 m/s where the flow is almost attached, Fig. 15 shows the spanwise flow in two opposite directions that meet at the baseline blade tip and trailing edge. Additionally, the skin friction lines show a similar flow behaviour for the baseline blade along the spanwise direction comparing to the blade with configurations 1 and 3, except at the blade tip.

At the blade tip, Fig. 15 shows that the skin friction lines are diffused from the blade tip to the trailing edge in the pressure and suction sides for configurations 1 and 3. In this way, the configurations 1 and 3 reduce wingtip vortices at the baseline blade tip. Accordingly, the wingtip vortices are generated on the tip and trailing edge of configurations 1 and 3 instead of a tip of the baseline blade as shown in Fig. 17.

Fig. 18 shows the streamlines at the top for the baseline as well as configurations 1 and 3. The comparison shows that configuration 3 can decrease wingtip vortices more than configuration 1. This is due to the difference in the tip chord reduction of configurations 3 and 1.

A similar conclusion can be drawn at 15 m/s where the suction side of a blade is dominated by the stalled flow (Figs. 16 and 19).

Fig. 20 shows different role of configurations 1 and 3 in the improvement of pressure distribution towards the span of the blade at the wind speed of 7m/s. Unlike configuration 3, improvement is obtained in the pressure distribution near the blade top for

Table 3
Optimisation study of the effect of winglet height and cant angle.

	Cant angle	Winglet Length	Percentage of increase/decrease in power (%)					
			Wind Speed (m/s)					
			5	7	10	15	20	25
Configuration (1)	90°	5 cm	3.5	3.8	5.3	−0.34	−5.5	−0.88
Rectangular (S809) airfoil		10 cm	5.0	6.3	9.5	7.9	−5.1	−3.3
		15 cm	5.4	6.7	7.1	−2.0	−6.0	−4.3
	45°	5 cm	5.1	5.1	5.4	2.0	−2.6	0.5
		10 cm	7.0	6.8	7.4	0.29	−3.5	−3.9
		15 cm	9.1	9.4	9.8	6.1	1.1	9.1
Configuration (2)	90°	5 cm	−2.5	−2.6	−4.6	−4.2	−4.0	−2.0
Rectangular (PSU94-097) airfoil		10 cm	−1.9	−1.3	−4.1	−9.1	−6.4	−1.6
		15 cm	0.3	−3.2	−4.3	−9.7	−7.4	−7.9
	45°	5 cm	0.43	−1.4	−4.9	−1.6	−0.5	−3.8
		10 cm	2.7	0.9	−3.7	−4.5	−3.0	−1.0
		15 cm	5.6	3.6	0.55	−7.2	4.2	5.8
Configuration (3)	90°	5 cm	1.6	−0.1	−3.7	−3.8	3.7	−0.05
Elliptical (S809) airfoil		10 cm	2.6	0.6	−3.0	−6.0	−3.2	−2.1
		15 cm	3.6	1.5	−2.0	−10.4	8.2	2.2
	45°	5 cm	0.8	−0.9	−4.8	−13.5	−3.3	−3.5
		10 cm	3.7	1.6	−2.2	−5.2	1.19	0.55
		15 cm	6.2	3.4	0.09	−11.1	−1.11	−1.85
Configuration (4)	90°	5 cm	0.7	−1.2	−5.3	−8.2	−8.0	−4.4
Elliptical (PSU94-097) airfoil		10 cm	2.0	0.06	−4.2	−13.4	−5.7	−2.6
		15 cm	3.3	1.3	−2.5	−8.4	2.8	−3.0
	45°	5 cm	1.0	−1.1	−4.5	−9.1	−5.6	4.0
		10 cm	3.7	1.5	−2.6	−8.5	4.7	−5.6
		15 cm	6.0	3.0	−1.7	−9.8	−4.8	−1.9

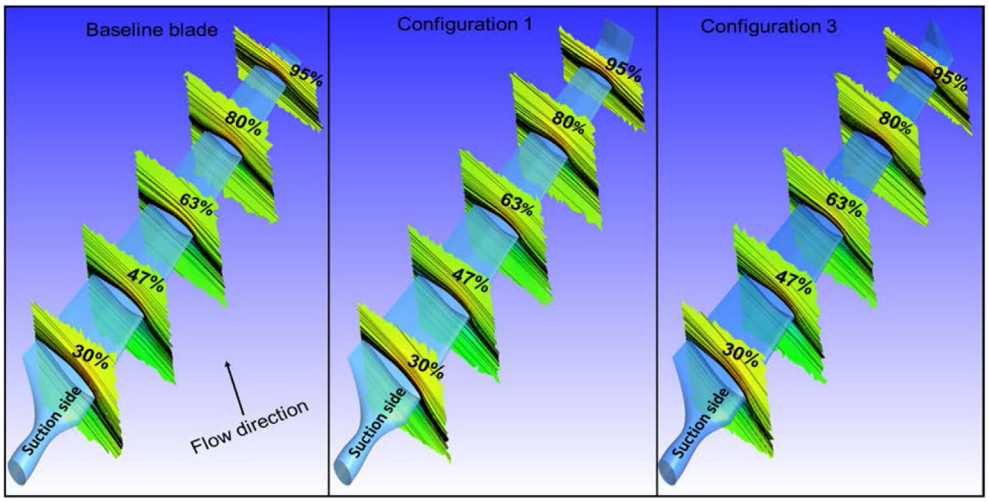

Fig. 13. Comparison of sectional flow streamlines between baseline blade and configurations (1, 3) at 7 m/s.

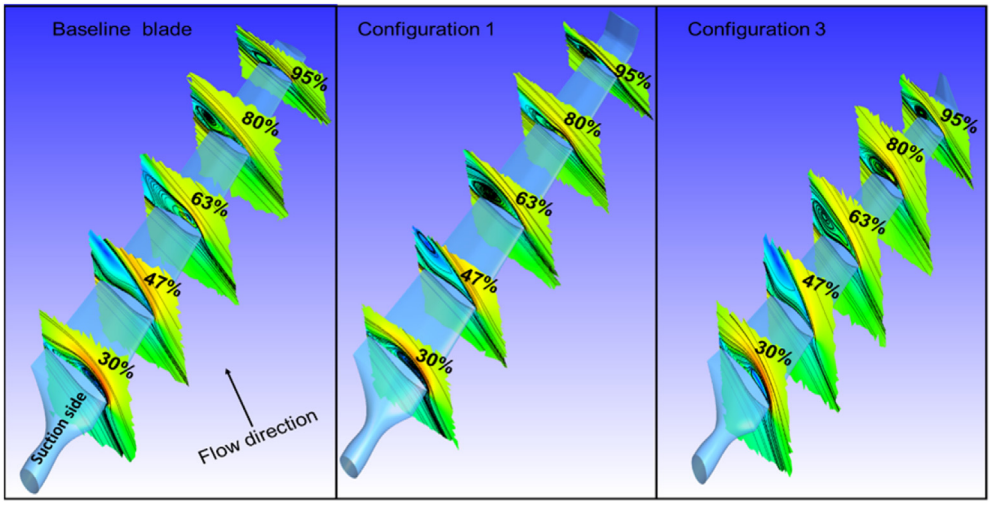

Fig. 14. Comparison of sectional flow streamlines between baseline blade and configurations (1, 3) at 15 m/s.

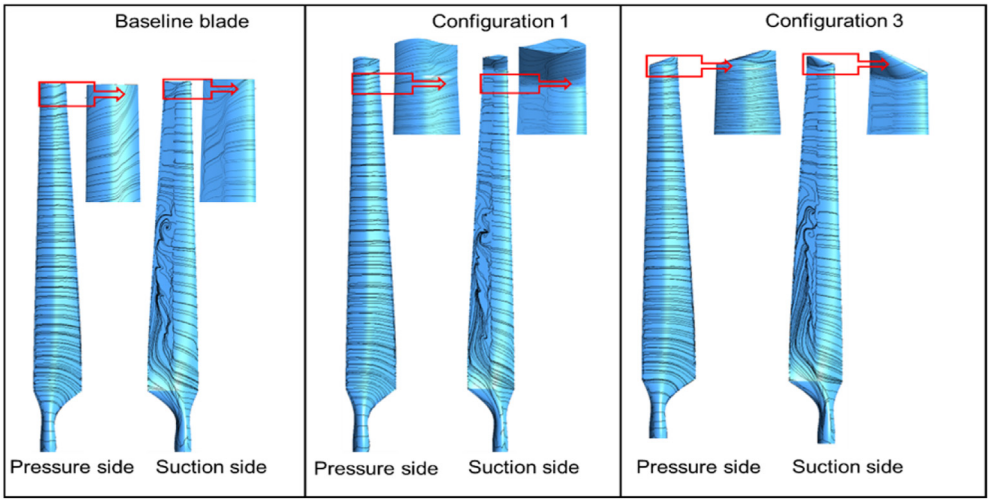

Fig. 15. Comparison of surface wall shear streamlines between baseline blade and configurations (1, 3) at 7 m/s.

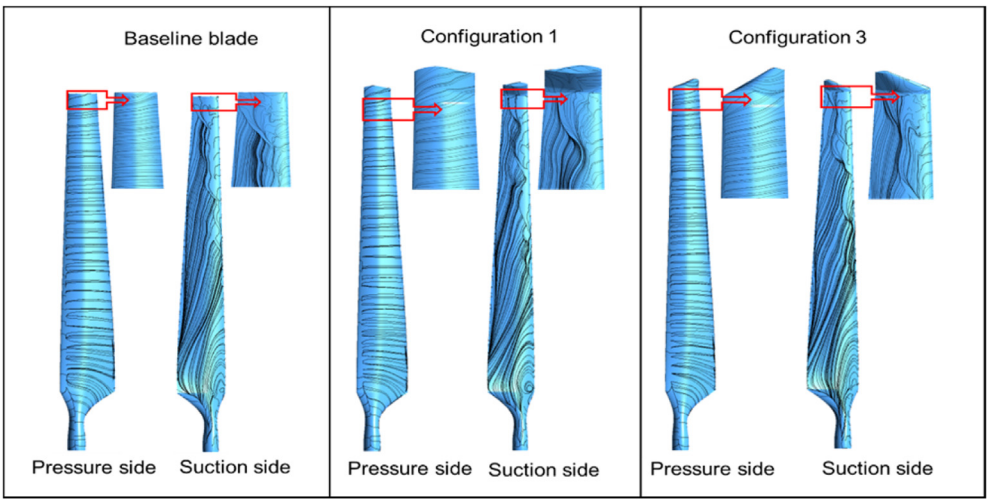

Fig. 16. Comparison of surface wall shear streamlines between baseline blade and configurations (1, 3) at 15 m/s.

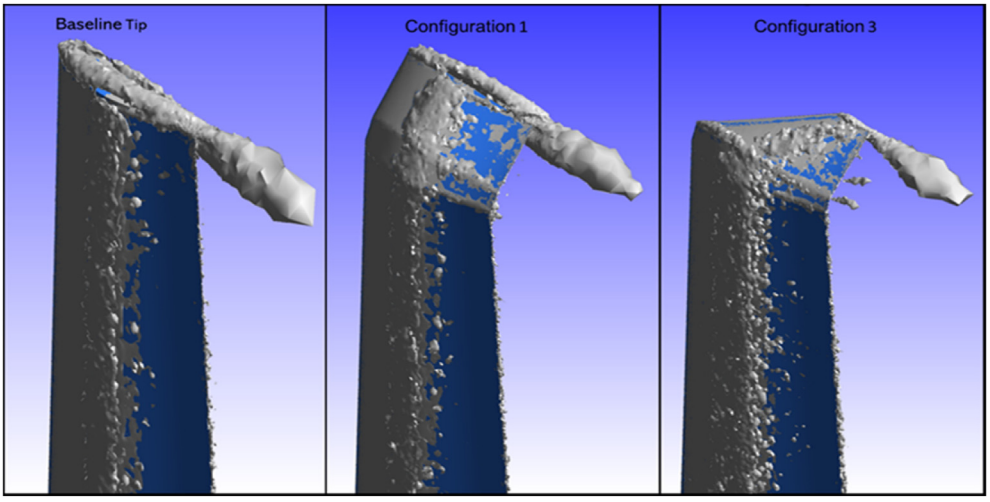

Fig. 17. Comparison of vorticity iso-surface at the blade tip region between baseline blade and configurations (1, 3) at 7 m/s.

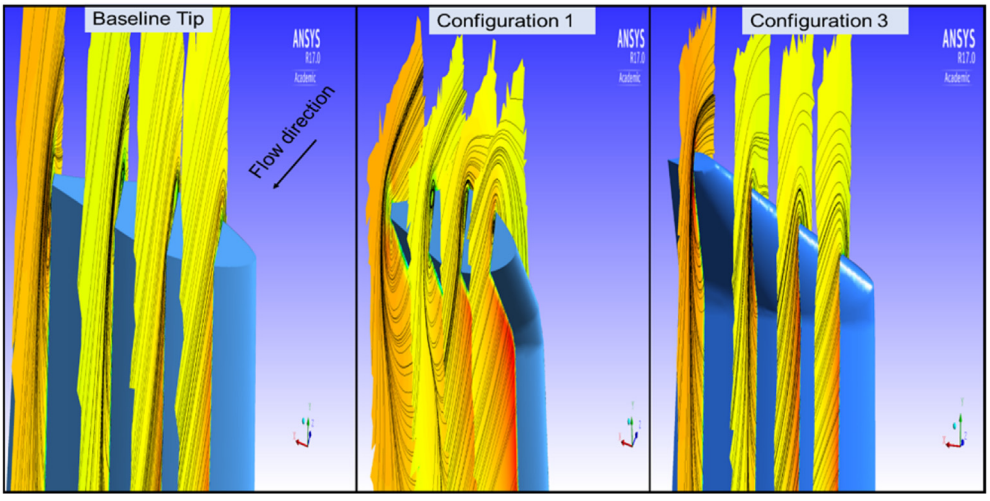

Fig. 18. Comparison of the tip streamlines between baseline blade and configurations (1, 3) at 7 m/s.

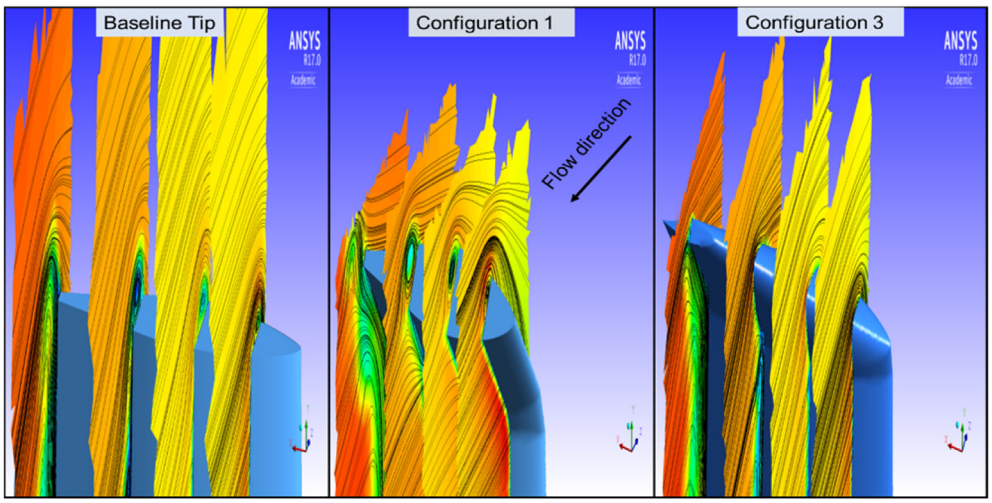

Fig. 19. Comparison of the tip streamlines between baseline blade and configurations (1, 3) at 15 m/s.

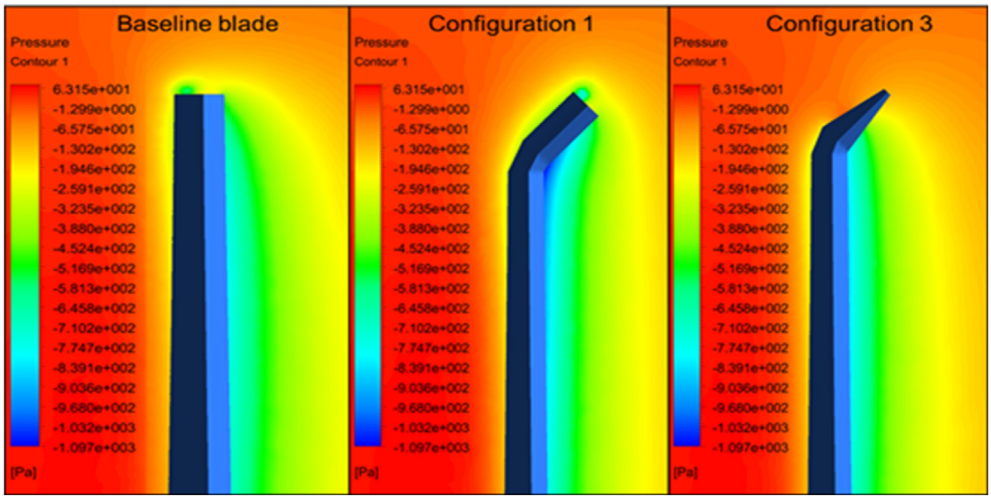

Fig. 20. Comparison of the pressure distribution of the baseline blade and configurations 1 and 3 at 7 m/s.

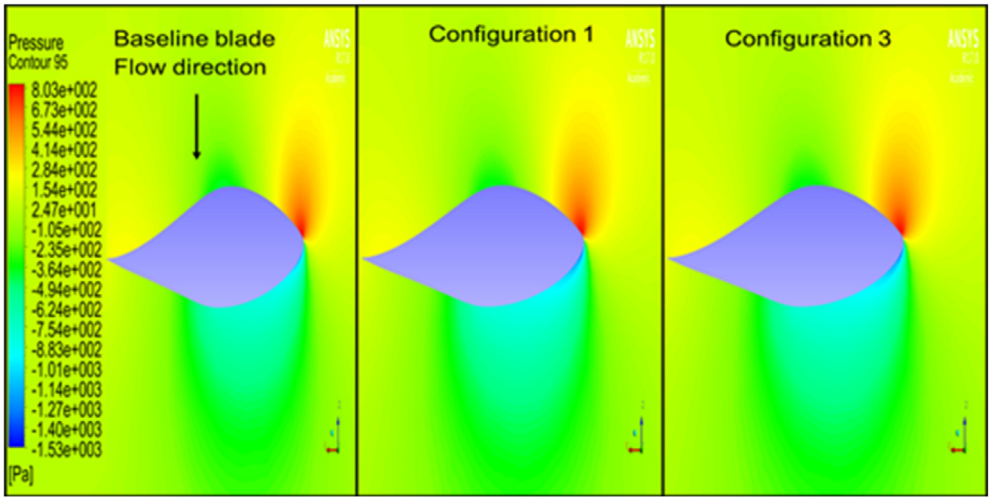

Fig. 21. Comparison of the sectional pressure distribution of the baseline blade and configurations 1 and 3 at 95% spanwise section of blade.

configuration 1. This improvement is clearly observed in the 95% and 98% spanwise sections of the modified blade when comparing to the baseline blade, as shown in Figs. 21 and 22, respectively. It is worth noting that the literature considered the winglets as diffusing devices which carry the wingtip vortices away from the rotor blade tip leading to an increase in the wind turbine performance. While in the current study, the comparative results between the rectangular and elliptical winglets reveal that an optimum extending (swept area) of a rotor can also be a reason behind an increase in the wind turbine power. Consequentially, among the winglet parameters, both of winglet length and cant angle are the most important parameters for improving the wind turbine performance.

8. Pressure coefficients

In order to understand the aerodynamic effect of the winglet function on the NREL phase VI production, comparisons of the calculated surface pressure coefficients were done between the baseline and the winglet configurations of 1 and 3 (Table 2) at wind speeds of 7 m/s, 10 m/s and 25 m/s as shown in Figs. 23–25. The pressure coefficient plots shown in Fig. 23 display that, the pressure coefficient distributions were improved on the spanwise suction side particularly on the sections that are located near the blade tip as the winglet was tilted toward the suction side. This improvement is clearly observed at 95% and 98% spanwise sections of the blade length. The improvement of the pressure coefficients suggests that, an additional energy can be extracted from the fluid flow by the rotor as a result of using winglets. When considering the effect of the winglet planform, Fig. 23 shows the configuration 1 results in more improvement in the pressure coefficients than the winglet configuration 3 on the suction sides. Similar conclusions can be drawn at 10 m/s and 25 m/s as shown in Figs. 24 and 25, respectively. The normal force coefficients C_n were also increased as compared to the baseline at 7 m/s, 10 m/s and 25 m/s wind speeds due to the influence of the winglet as shown in Figs. 23–25.

9. Power and thrust force

Table 4 shows the results of the percentage of increase/decrease in the output power and thrust force using four different winglet configurations. The table shows that, the maximum increase in the output power was achieved by configuration 1. Fig. 26 shows the change in the output power of the NREL phase VI for the four configurations. Configuration 1 causes an increase in output power by more than 9% at the wind speeds of 5–10 m/s where the fluid flow regime is attached. On the other hand, the increase in the performance of this configuration reduced to 6% and 1% at wind speeds of 15 m/s and 20 m/s, respectively, where the flow is in the stall regime. In addition, the NREL phase VI rotor is designed to improve the power production at wind speeds of more than 20 m/s as shown in experimental data in Fig. 5. Accordingly, the winglet configuration 1 led to an increase in the performance by 9.1% at the wind speed of 25 m/s (Fig. 26) due to an improvement in the pressure coefficients as explained previously. However, at this wind speed other winglet configurations caused an increase in output power less than that of configuration 1.

The performance of configurtaion 1 is compared with the winglet design created by Elfarra, Sezer-Uzol [40] as shown in Fig. 27. This winglet is generated by 7.5 cm extension of the blade towards the suction side by a cant angle of 84° and twisted angle of 2°. It can be seen that at low wind speeds Elfarra's winglet performs better than configuration 1. However, at the wind speeds higher than 22.5 m/s, configuration 1 has better performance than the Elfarra's winglet.

Furthermore, Table 4 shows that, the maximum increase in the thrust force is obtained by attaching winglet configuration 1. A comparison of the blade thrust force for the baseline and configuration 1 (rectangular winglet with S809) is also shown in Fig. 28. The main disadvantage of the thrust force increase is possible tip deflection due to an increase in the flapwise bending moment. Nevertheless, the increase in the thrust force predicted for configuration 1 is not a great concern for a safe operation of the wind turbine.

10. Conclusions

In this study, two different winglet planforms, rectangular and elliptical, were numerically tested using CFD to investigate their effect on the wind turbine performance. Two airfoils, S809 and PSU 94–097, were chosen to create different winglet profiles. The NREL phase VI rotor was chosen to validate the baseline CFD simulations as there is experimental data available for this case. The optimisation study reveals that 15 cm height with 45° cant angle are the best parameters for winglet configurations.

The elliptical planform reduces the effect of the wingtip vortices

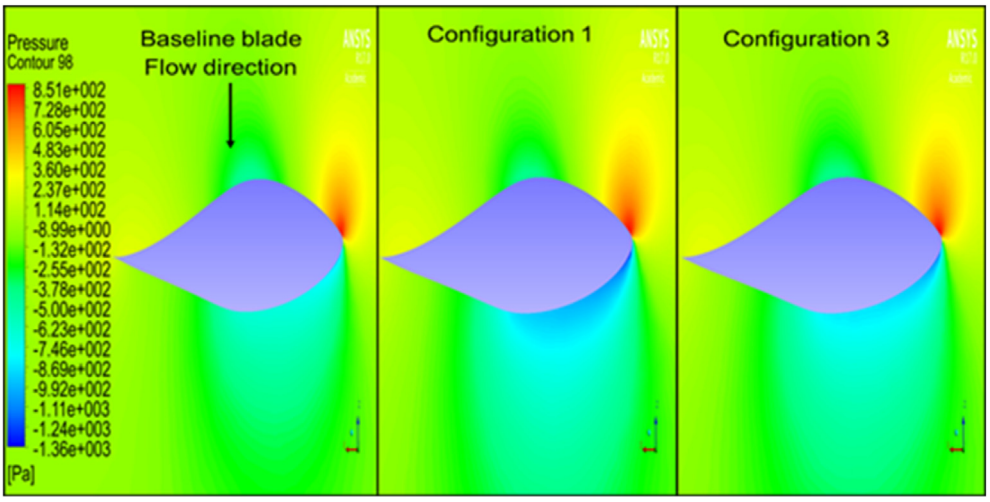

Fig. 22. Comparison of the sectional pressure distribution of the baseline blade and configurations 1 and 3 at 98% spanwise section of balde.

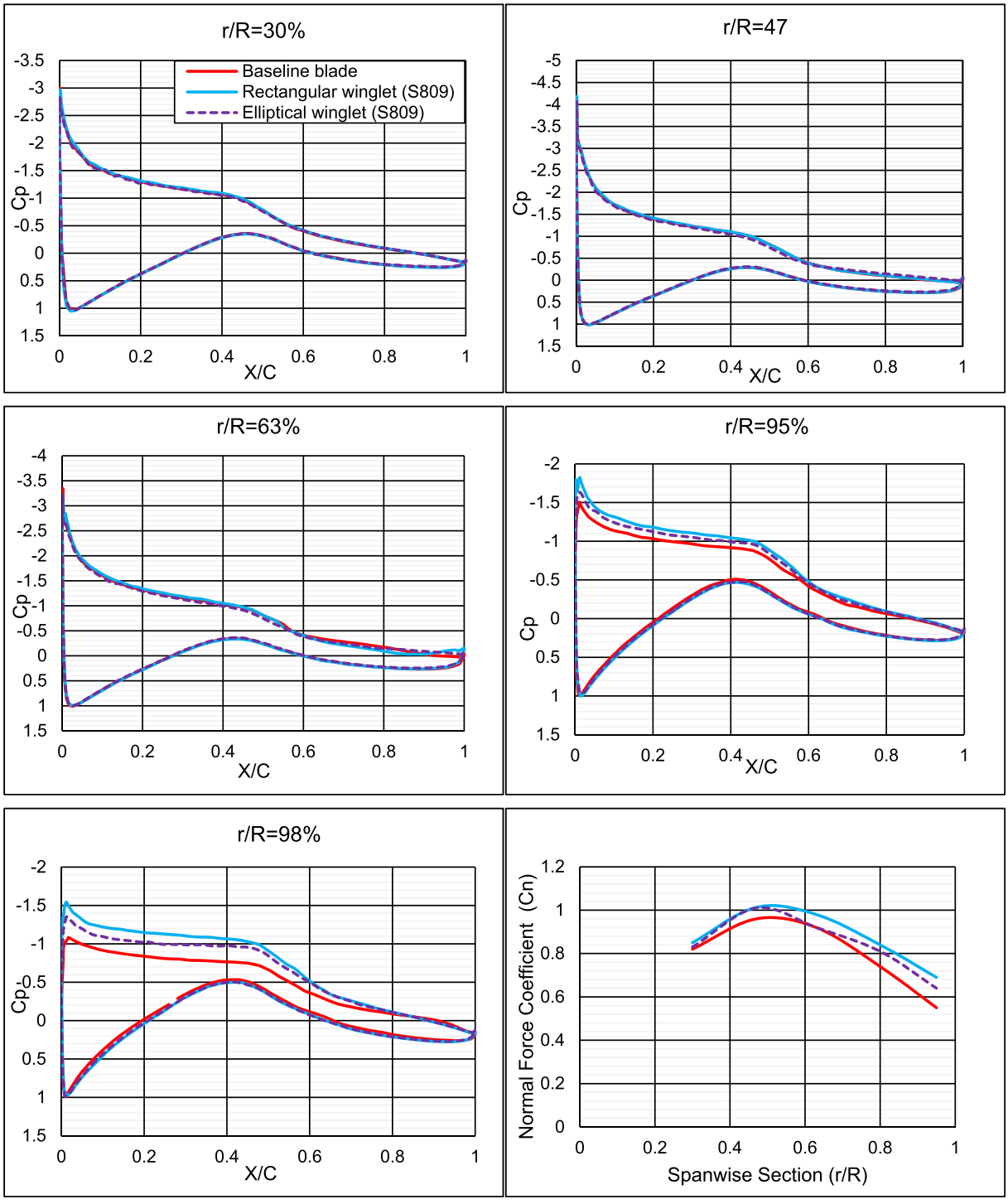

Fig. 23. Comparison of CFD and measured coefficients (pressure and normal force) using winglet at 7 m/s.

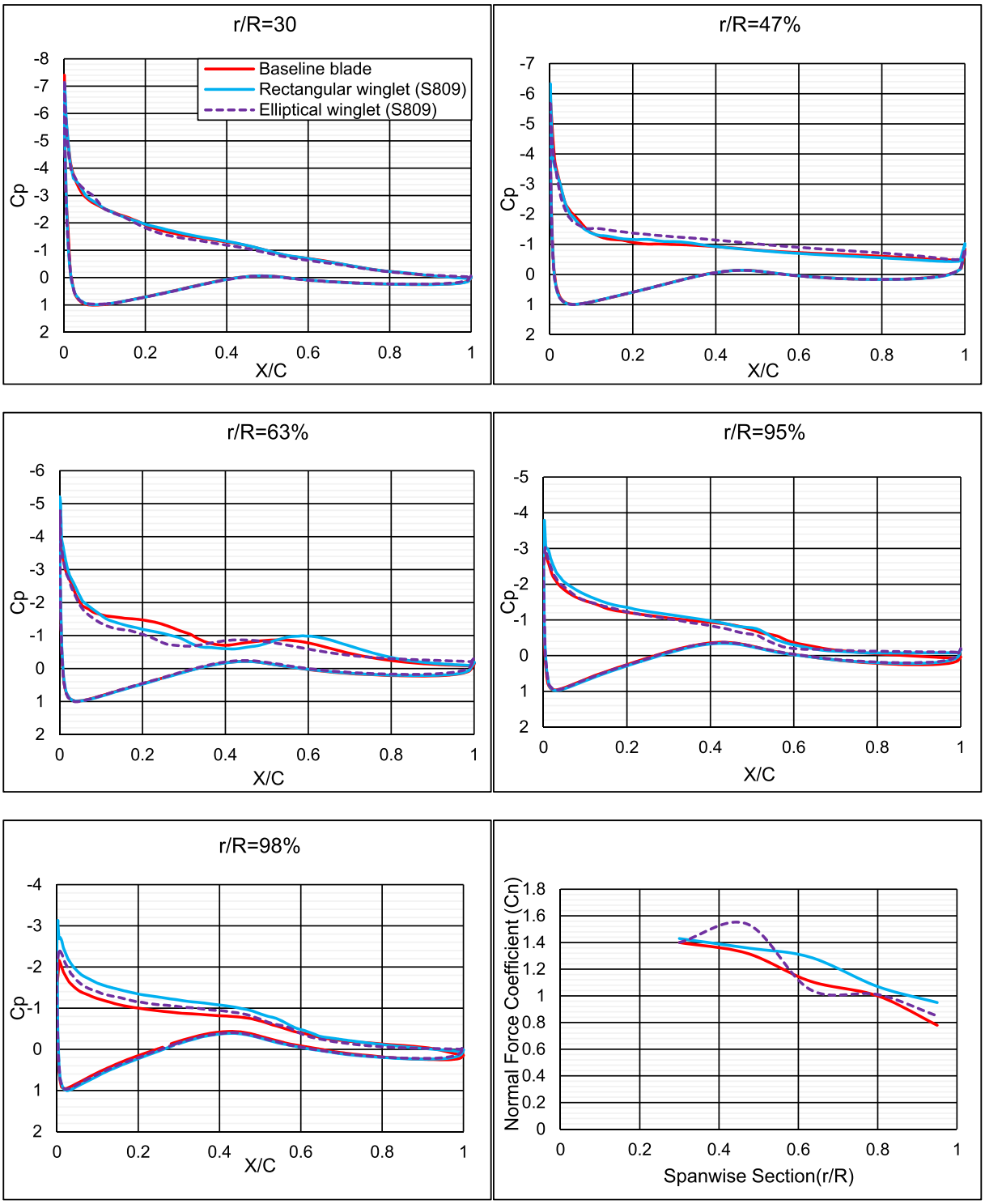

Fig. 24. Comparison of CFD and measured coefficients (pressure and normal force) using winglet at 10 m/s.

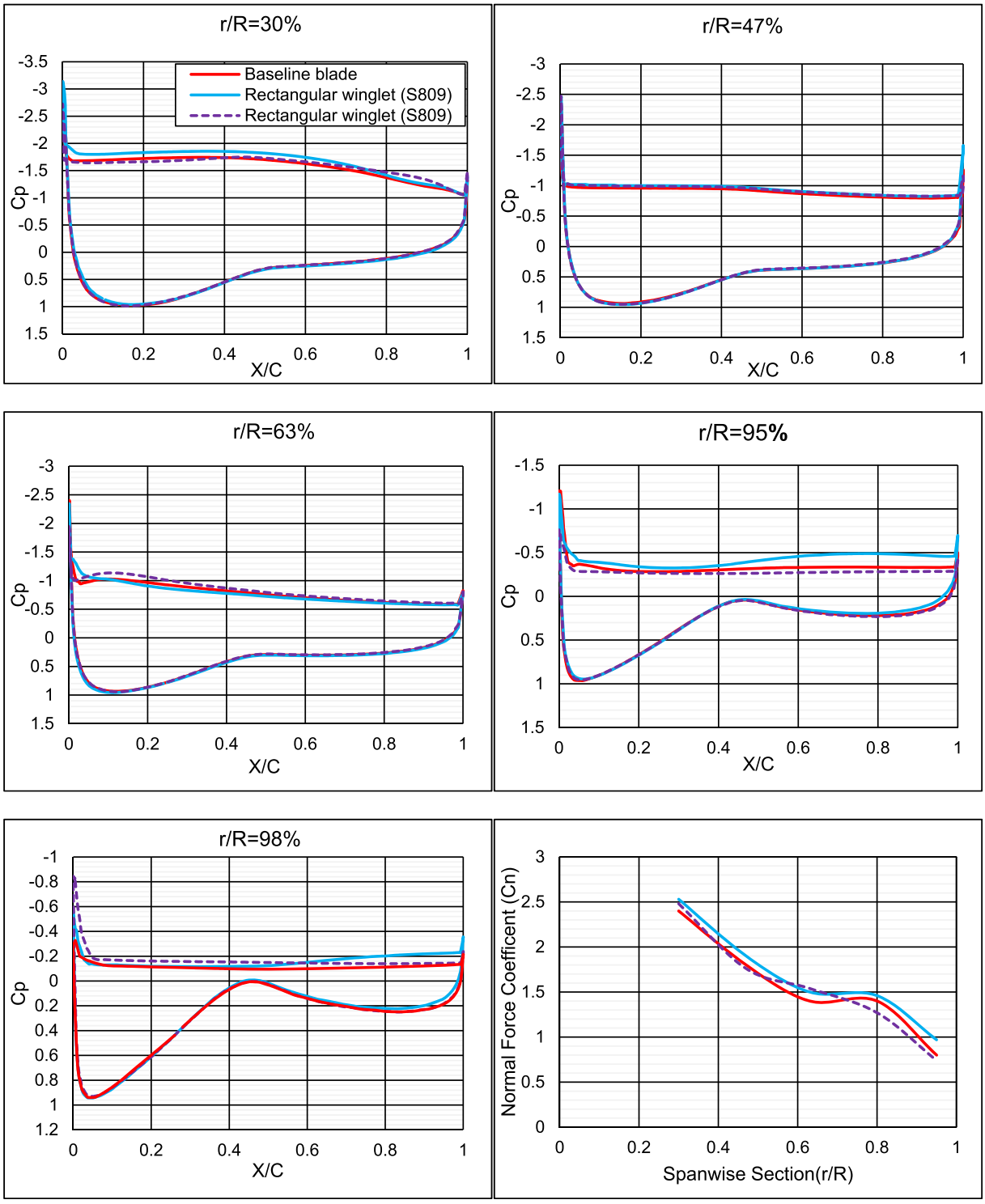

Fig. 25. Comparison of CFD and measured coefficients (pressure and normal force) using winglet at 25 m/s.

Table 4
Increase in the power and thrust force using different winglet configurations.

Wind Speed (m/s)	Rectangular Winglet Cant angle 45°/h = 15 cm				Elliptical Winglet Cant angle 45°/h = 15 cm			
	Winglet airfoil S809 (1)		Winglet airfoil PSU 94–097 (2)		Winglet airfoil S809 (3)		Winglet airfoil PSU 94–097 (4)	
	Power (%)	Thrust (%)	Power (%)	Thrust (%)	Power (%)	Thrust (%)	Power (%)	Thrust (%)
5	9.1	10.3	5.6	9.5	6.2	5.9	6.0	7.6
7	9.4	9.6	3.6	6.6	3.4	3.9	3.0	4.6
10	9.8	6.9	0.55	3.9	0.09	1.4	−1.7	1.7
15	6.1	5.9	−7.2	4.9	−11.1	1.6	−9.8	2.6
20	1.1	2.7	4.2	2.0	−1.11	0.3	−4.8	−0.3
25	9.1	3.3	5.8	1.8	−1.85	−0.47	−1.9	−0.05

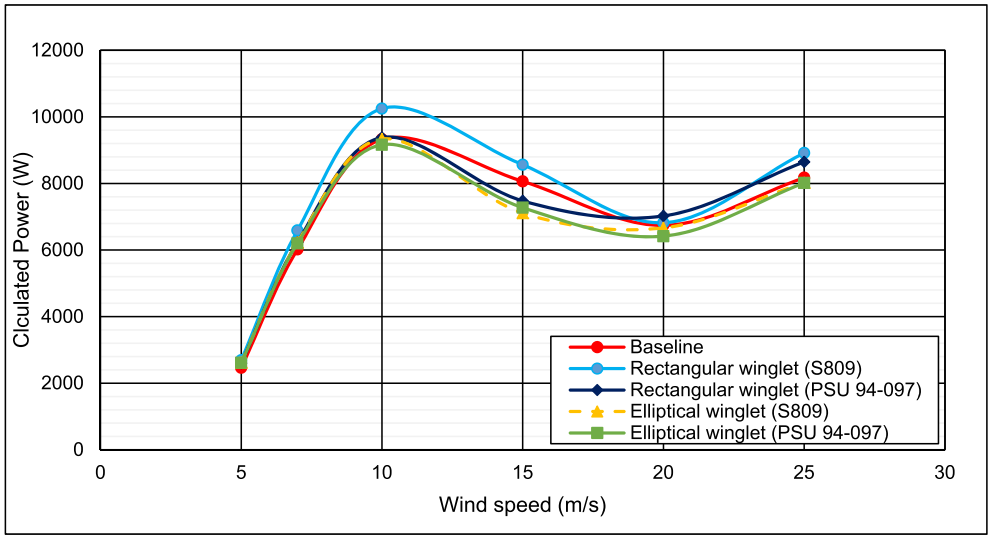

Fig. 26. Comparison of calculated power using different winglet designs with the baseline.

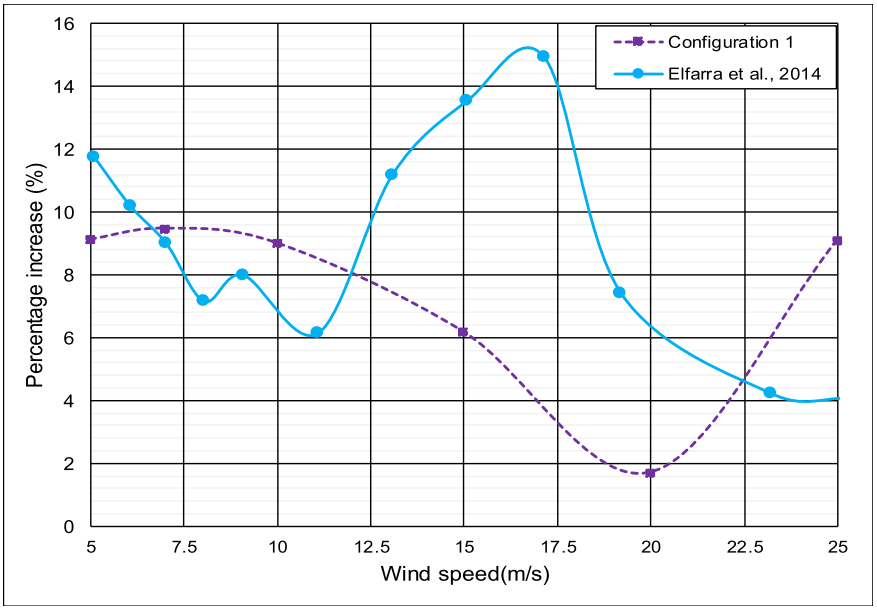

Fig. 27. Comparison of the percentage of power increase of configuration 1 with the literature.

more than rectangular one due to the reduction in the tip for elliptical case. However, the improvements of the pressure coefficients near the blade tip reveal the superiority of rectangular planform for extracting more energy than as compared to the elliptical winglet. Accordingly, the extended area that is added to the turbine blade causes an improvement in the performance more than weakening the effect of the wingtip vortices as shown in Figs. 18 and 19. Further, the numerical results show for the winglet

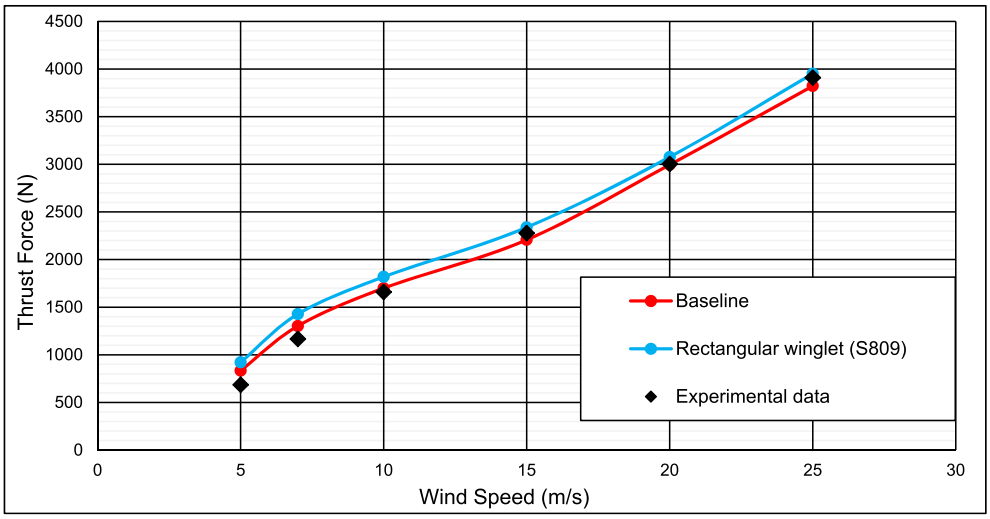

Fig. 28. Comparison of calculated blade thrust force for the baseline and with rectangular winglet with the experimental data (baseline only).

the S809 airfoil has potential to improve the NREL phase VI performance better than the PSU 94–097 airfoil. Hence, winglet planform and airfoil both play significant roles in influencing the wind turbine performance and thrust force. Overall it is found that configuration 1 (rectangular winglet with airfoil S809) results in the best increase in the performance of the NREL phase VI rotor. However, it should be noted that the successful winglet design is significantly affected by the operating conditions for each wind turbine such as Reynolds number, turbulence and flow separation. Therefore, there is an optimum winglet design that has a potential to improve the performance of wind turbine at each operating condition.

Acknowledgement

The authors are grateful to the Iraqi Ministry of Higher Education and Scientific Research for supporting the study.

References

[1] GWEC, Global Wind Report, 2016.
[2] H. Snel, R. Houwink, J. Bosschers, Sectional Prediction of Lift Coefficients on Rotating Wind Turbine Blades in Stall, Netherlands Energy Research Foundation Petten, Netherlands, 1994.
[3] J.F. Manwell, J.G. McGowan, A.L. Rogers, Wind Energy Explained: Theory, Design and Application, John Wiley & Sons, 2010.
[4] T. Burton, et al., Wind Energy Handbook, John Wiley & Sons Ltd, West Sussex, England, 2001.
[5] X. Tang, Aerodynamic Design and Analysis of Small Horizontal axis Wind Turbine Blades, University of Central Lancashire, UK, 2012.
[6] C. Lindenburg, in: Investigation into Rotor Blade Aerodynamics, Netherlands Society for Energy and the Environment, 2003. Paper ECN-C-03-025.
[7] C. Zhang, Aerodynamic, Structural and Aero-elasticity Modelling of Large Composite Wind Turbine Blades, Loughborough University, 2013.
[8] D. Wood, A three-dimensional analysis of stall-delay on a horizontal-axis wind turbine, J. Wind Eng. Ind. Aerod. 37 (1) (1991) 1–14.
[9] H. Snel, et al., Sectional prediction of 3D effects for stalled flow on rotating blades and comparison with measurements, in: Proc. European Community Wind Energy Conference, 1993.
[10] C.E. Carcangiu, CFD-RANS Study of Horizontal axis Wind Turbines, Universita'degli Studi di Cagliari, 2008.
[11] W.Z. Shen, et al., Tip loss corrections for wind turbine computations, Wind Energy 8 (4) (2005) 457–475.
[12] L. Vermeer, J.N. Sørensen, A. Crespo, Wind turbine wake aerodynamics, Prog. Aero. Sci. 39 (6) (2003) 467–510.
[13] E. Branlard, Wind Turbine Tip-loss Corrections: Review, Implementation and Investigation of New Models, RisøDUT (Technical University of Denmark), Lyngby, Denmark, 2011.
[14] J.G. Leishman, Challenges in modelling the unsteady aerodynamics of wind turbines, Wind Energy 5 (2-3) (2002) 85–132.
[15] S. Gupta, Development of a Time-accurate Viscous Lagrangian Vortex Wake Model for Wind Turbine Applications, University of Maryland, 2006.
[16] M.D. Maughmer, Design of winglets for high-performance sailplanes, J. Aircraft 40 (6) (2003) 1099–1106.
[17] M. Maughmer, P. Kunz, Sailplane winglet design, Tech. Soar. 22 (4) (1998) 116–123.
[18] D.P. Gertz, An Evaluation Testbed for Alternative Wind Turbine Blade Tip Designs, University of Waterloo, 2011.
[19] M.A. Elfarra, N. Sezer Uzol, I.S. Akmandor, Investigations on blade tip tilting for Hawt rotor blades using CFD, Int. J. Green Energy 12 (2) (2015) 125–138.
[20] A. Gupta, R. Amano, CFD Analysis of Wind Turbine Blade with Winglets, 2012. ASME Paper No. DETC2012-70679.
[21] P.M. Congedo, M.G. De Giorgi, Optimizing of a wind turbine rotor by CFD modeling, in: ANSYS Italy Conference, 2008 (Mestre, Italy).
[22] J. Johansen, N.N. Sørensen, Numerical analysis of winglets on wind turbine blades using CFD, in: 2007 European Wind Energy Conference and Exhibition, 2007.
[23] A. Ali, Aerodynamic Optimisation of Small Scale Horizontal axis Wind Turbine Blades, RMIT University, Melbourne, Australia, 2014.
[24] M.H. Ariffudin, et al., Effectiveness of blade tip on low speed horizontal Axis wind turbine performance, Jurnal Teknologi 78 (8–4) (2016) 31–39.
[25] M. Hand, et al., Unsteady Aerodynamics Experiment Phase VI: Wind Tunnel Test Configurations and Available Data Campaigns, National Renewable Energy Lab., Golden, CO.(US), 2001.
[26] D. John, J. Anderson, in: Computational Fluid Dynamics: the Basics with Applications, P. Perback, International ed., 1995. Published.
[27] F. Fluent, ANSYS FLUENT 12.0 User's Guide, 2009.
[28] A. Sudhamshu, et al., Numerical study of effect of pitch angle on performance characteristics of a HAWT, Eng. Sci. Technol. 19 (1) (2016) 632–641.
[29] R. Lanzafame, S. Mauro, M. Messina, Wind turbine CFD modeling using a correlation-based transitional model, Renew. Energy 52 (2013) 31–39.
[30] M.M. Yelmule, E.A. Vsj, CFD predictions of NREL phase VI rotor experiments in NASA/AMES wind tunnel, Int. J. Renew. Energy Resour. 3 (2) (2013) 261–269.
[31] E. Sagol, M. Reggio, A. Ilinca, Assessment of two-equation turbulence models and validation of the performance characteristics of an experimental wind turbine by CFD, ISRN Mech. Eng. 2012 (2012).
[32] F.R. Menter, Review of the shear-stress transport turbulence model experience from an industrial perspective, Int. J. Comput. Fluid Dynam. 23 (4) (2009) 305–316.
[33] F.R. Menter, Improved Two-equation K-omega Turbulence Models for Aerodynamic Flows, 1992.
[34] M.A. Potsdam, D.J. Mavriplis, Unstructured mesh CFD aerodynamic analysis of the NREL Phase VI rotor, AIAA Paper 1221 (2009) 2009.
[35] Y. Li, et al., Dynamic overset CFD simulations of wind turbine aerodynamics, Renew. Energy 37 (1) (2012) 285–298.
[36] D.M. Somers, Design and Experimental Results for the S809 Airfoil, National Renewable Energy Lab., Golden, CO (United States), 1997.
[37] M. Maughmer, T. Swan, S. Willits, The design and Testing of A Winglet Airfoit for low-speed Aircraft, Tech. Soar. 26 (3) (2002) 76–88.
[38] D.P. Gertz, An Evaluation Testbed for Alternative Wind Turbine Blade Tip Designs, University of Waterloo, 2011.
[39] D. Maniaci, Wind Turbine Design Using a Free-wake Vortex Method with Winglet Application, Pennsylvania State University, 2013.
[40] M.A. Elfarra, N. Sezer-Uzol, I.S. Akmandor, NREL VI rotor blade: numerical investigation and winglet design and optimization using CFD, Wind Energy 17 (4) (2014) 605–626.